Eur. Phys. J. C (2025) 85:703
https://doi.org/10.1140/epjc/s10052-025-14338-z

THE EUROPEAN
PHYSICAL JOURNAL C

Regular Article - Theoretical Physics

Neutrino oscillation tomography of the Earth with the Hyper-Kamiokande detector

C. Jesús-Valls[1,a], **S. T. Petcov**[1,2,3], **J. Xia**[1]

[1] Kavli IPMU (WPI), UTIAS, The University of Tokyo, Kashiwa, Chiba 277-8583, Japan
[2] INFN/SISSA, Via Bonomea 265, 34136 Trieste, Italy
[3] Institute of Nuclear Research and Nuclear Energy, Bulgarian Academy of Sciences, 1784 Sofia, Bulgaria

Received: 28 January 2025 / Accepted: 21 May 2025

Abstract Using PREM as a reference model for the Earth density distribution we investigate the sensitivity of the Hyper-Kamiokande (HK) detector to deviations of the Earth (i) core average density $\bar{\rho}_C$, (ii) lower mantle average density $\bar{\rho}_{lman}$) and (iii) upper mantle average density $\bar{\rho}_{uman}$, from their respective PREM densities. The analysis is performed by studying the effects of the Earth matter on the oscillations of atmospheric ν_μ, ν_e, $\bar{\nu}_\mu$ and $\bar{\nu}_e$. We implement the constraints on the variations of ρ_C, ρ_{lman} and ρ_{uman} following from the precise knowledge of the Earth mass $M_\oplus$ and moment of inertia $I_\oplus$, as well as from the requirement that the Earth be in hydrostatic equilibrium (EHE). These constraints limit in the case of the three layer Earth density structure we are considering the maximal positive deviation of $\bar{\rho}_C$ from its PREM value to 10%. Considering the case of normal ordering (NO) of neutrino masses, we present results which illustrate the dependence of sensitivity to the core, lower and upper mantle average densities on the energy and zenith angle resolutions and on the value of θ_{23}. We show, in particular, that in the "nominal" case of neutrino energy resolution $E_{res} = 30\%$ and zenith angle resolution $\theta_{zres} = 20°$ and for, e.g., $\sin^2\theta_{23} = 0.45$ (0.58), HK can determine the average core density $\bar{\rho}_C$ at 2σ C.L. after 6500 days of operation with an uncertainty of (−14.5%)/+39.5% ((−9.3%/+31.7%). In the "more favorable" case of $E_{res} = 20\%$ and $\theta_{zres} = 10°$, and if $\sin^2\theta_{23} = 0.58$ (0.45), the core density would be determined at 2σ C.L. with an uncertainty of (−8.3%)/+9.8% ((−9.2%)/+11.3%).

1 Introduction

Our current knowledge of the density structure and composition of the Earth's interior is based primarily on seismological and geophysical data (see, e.g., [1–9]). These data were used to construct the Preliminary Reference Earth Model (PREM) [10] of the density distribution of the Earth. According to the PREM model, the Earth density distribution ρ_{E} is spherically symmetric, $\rho_{\mathrm{E}} = \rho_{\mathrm{E}}(r)$, r being the distance from the Earth center, and there are three major density structures or layers - the inner core, outer core and the mantle, and a certain number of substructures (shells). There are also three thin "surface" layers just below the Earth surface - the ocean and the two crust layers. The mantle has five shells in the model. The mean Earth radius is $R_\oplus = 6371$ km; the Earth inner core (IC) and outer core (OC) have radii $R_{IC} = 1221.5$ km and $R_{OC} = 3480$ km. The mantle layer is located between the outer core and the lower crust layer, i.e., for r in the interval $R_{\mathrm{C}} \leq r \leq R_{\mathrm{man}}$, with $R_{\mathrm{man}} = 6346.6$ km.

The determination of the radial density distributions in the mantle, outer core and inner core (or core) $\rho_{\mathrm{man}}(r)$, $\rho_{\mathrm{OC}}(r)$ and $\rho_{\mathrm{IC}}(r)$ (or $\rho_{\mathrm{C}}(r)$) from seismological and geophysical data is not direct and suffers from uncertainties [2–5]. It requires the knowledge, in particular, of the seismic wave speed velocity distributions in the interior of the Earth, which depends on the pressure, temperature, composition and elastic properties of the Earth's interior that are not precisely known. Perhaps a rather conservative estimate of the uncertainty in the knowledge of $\rho_{man}(r)$ is $\sim 5\%$; for the core density $\rho_c(r)$ it is larger and can be noticeably larger [2–5].

A precise knowledge of the Earth's density distribution and of the average densities of the mantle, outer core and inner core, or the core, is crucial for understanding the physical conditions and basic aspects of the structure and properties of the Earth's interior (including the dynamics of mantle and core, the bulk composition of the Earth's three structures, the generation, properties and evolution of the Earth's magnetic field and the gravity field of the Earth) [1,2,11,12].

---

[a] e-mail: cesar.jesus@cern.ch (corresponding author)

Unique alternative methods of obtaining information about the density profile of the Earth are the neutrino absorption and neutrino oscillation tomographies of the Earth. The propagation and oscillations of the active flavour neutrinos and antineutrinos ν_l and $\bar{\nu}_l$, $l = e, \mu, \tau$, in the Earth are affected by the Earth matter. The original idea of neutrino absorption Earth tomography is based on the observation that the cross section of the neutrino-nucleon interaction rises with energy. For neutrinos with energies $E_\nu \gtrsim$ a few TeV, the inelastic scattering off protons and neutrons leads to absorption of neutrinos and thus to attenuation of the initial neutrino flux. The magnitude of the attenuation depends on the Earth matter density along the neutrino path. Attenuation data for neutrinos with different path-lengths in the Earth carry information about the matter density distribution in the Earth interior. The absorption method of Earth tomography with accelerator neutrino beams, which is difficult (if not impossible) to realise in practice was discussed first in [13,14] and later in grater detail in [15–26].

The oscillations between the active flavour neutrinos and antineutrinos, $\nu_l \leftrightarrow \nu_{l'}$ and $\bar{\nu}_l \leftrightarrow \bar{\nu}_{l'}$, $l, l' = e, \mu$, having energies in the range $E \sim (0.1 - 15.0)$ GeV and traversing the Earth, can be strongly modified by the Earth matter effects (see, e.g., [27]). These modifications depend on the Earth matter density along the path of the neutrinos.[1] Thus, by studying the effects of Earth matter on the oscillations of, e.g., ν_μ and ν_e ($\bar{\nu}_\mu$ and $\bar{\nu}_e$) neutrinos traversing the Earth along different trajectories it is possible to obtain information about the Earth density distribution.

Atmospheric neutrinos (see, e.g., [35,36]) are a perfect tool for performing Earth tomography. Consisting of significant fluxes of muon and electron neutrinos and antineutrinos, ν_μ, ν_e, $\bar{\nu}_\mu$ and $\bar{\nu}_e$, produced in the interactions of cosmic rays with the Earth atmosphere, they have a wide range of energies spanning the interval from a few MeV to multi-GeV to multi-TeV. Being produced isotropically in the upper part of the Earth atmosphere at a height of $\sim$ 15 km, they travel distances from $\sim$ 15 km to 12,742 km before reaching detectors located on the Earth surface, crossing the Earth along all possible directions and thus "scanning" the Earth interior. The interaction rates that allow to get information about the Earth density distribution can be obtained in the currently taking data IceCube experiment [37–40] and its planned upgrade [40], in the ORCA [41], Hyper Kamiokande [42,43] and DUNE [44] experiments which are under construction, and in the planned INO [45] experiment.

In 2018 in [32] the authors, following the idea of performing absorption neutrino tomography of the Earth with atmospheric neutrinos put forward in [26], used the data of the IceCube experiment on multi-TeV atmospheric ν_μ and $\bar{\nu}_\mu$ with sufficiently long paths in the Earth [46] and obtained information about the Earth density distribution. Their results, although not very precise, broadly agree with the PREM model. In particular, they contain evidence at 2σ C.L. that the core is denser than the mantle. The authors used the IceCube data to "weight" the Earth with neutrinos: the value of the Earth mass found in [32], $M_\oplus^\nu = (6.0^{+1.6}_{-1.3}) \times 10^{24}$ kg, is in good agreement with gravitationally determined value [47,48], $M_\oplus = (5.9722 \pm 0.0006) \times 10^{24}$ kg. This was the first time the study of neutrinos traversing the Earth provided information of the Earth interior and marked the beginning of real experimental data driven neutrino tomography of the Earth.

The neutrino oscillation tomography of the Earth with IceCube, ORCA, DUNE and INO detectors is discussed in [33,34,49–59] (the early studies include [60,61] briefly described in [53]; see also [62]).

In the present article we investigate the possibility to get information about the Earth density structure performing neutrino tomography of the Earth with the Hyper-Kamiokande (HK) experiment by studying the oscillations of atmospheric neutrinos (antineutrinos) ν_μ and ν_e ($\bar{\nu}_\mu$ and $\bar{\nu}_e$) with different energies and pathlengths in the Earth. In [42,43] the HK collaboration presented results on the potential of the HK experiment to determine the composition (i.e., the Z/A ratio) of the Earth core by using neutrino oscillation tomography of the Earth. The Hyper-Kamiokande detector is under construction and is foreseen to begin to take data in 2027.

The article is organised as follows. In Sect. 2 we review basic elementary particle and geophysics aspects of the study we perform. In particular, in Sect. 2.1 we discuss in detail the implementation of the Earth total mass, moment of inertia and hydrostatic equilibrium constraints in our analysis. Section 3 is devoted to the analysis methodology (including discussions of HK simulation, event selection, the employed atmospheric neutrino fluxes, oscillation probabilities evaluation, enhanced datasets generation and sensitivity calculation). In Sect. 4 we present the results of our analysis of HK sensitivity to the Earth density structure. Section 5 contains our conclusions.

---

[1] More precisely, they depend on the electron number density $N_e(r)$, $N_e(r) = \rho_{\rm E}(r) Y_e(r)/m_N$, $Y_e(r)$ and m_N being the electron fraction number and nucleon mass. It follows from the studies of the Earth matter composition that $Y_e \cong (0.490 - 0.496)$ in the mantle and $Y_e \cong (0.466-0.471)$ in the core (see, e.g., [28–31]). Taking into account these uncertainties has no effect on the results on the densities of the mantle and the core obtained in neutrino tomography studies (see, e.g.,[32]). The relation between $N_e(r)$ and $\rho_{\rm E}(r)$ can be used to obtain information about $Y_e(r)$, i.e., the composition of the core and mantle layers of the Earth (see, e.g., [33,34]).

2 PREM input, oscillation probabilities and Earth data constraints

We use the PREM model as a reference model of the Earth density distribution $\rho_{\rm E}(r)$ and assume that the location of the mantle-core and the outer core-inner core boundaries are correctly described by the model. In the PREM model, as we have already briefly discussed in the Introduction, the Earth density distribution $\rho_{\rm E}$ is assumed to be spherically symmetric, $\rho_{\rm E} = \rho_{\rm E}(r)$, r being the distance from the Earth center. The mean Earth radius is $R_\oplus = 6371$ km; the Earth core (C) has a radius of $R_C = 3480$ km with the inner core (IC) and outer core (OC) extending respectively from $r = 0$ to $r = R_{IC} = 1221.5$ km, and from $r = 1221.5$ km to $r = R_{OC} = R_C = 3480$ km. The mean densities of the mantle, IC, OC and core are respectively $\bar{\rho}_{\rm man} = 4.66$ g/cm^3, $\bar{\rho}_{\rm IC} = 12.89$ g/cm^3, $\bar{\rho}_{\rm OC} = 10.90$ g/cm^3 and $\bar{\rho}_{\rm C} = 10.99$ g/cm^3. If we include the three "surface" layers in the mantle, as we are going to do in what follows, the mantle extends from $r = R_C = 3480$ km to $r = R_\oplus = 6371$ km and the mean density of the mantle changes to $\bar{\rho}_{\rm manco} = 4.45$ g/cm^3 (see, e.g., [63]). The change of density between the mantle and the outer core is described by a step function.

For a spherically symmetric Earth density distribution, the neutrino trajectory in the Earth is specified by the value of the zenith angle θ_z of the trajectory. For $90^\circ \leq \theta_z \leq (180^\circ - 33.17^\circ)$, or path lengths $L \geq 10665.7$ km, neutrinos cross the Earth core. The path length for neutrinos which cross only the Earth mantle is given by $L = -2R_\oplus \cos\theta_z$. If neutrinos cross the Earth core, the lengths of the paths in the mantle, $2L^{\rm man}$, and in the core, $L^{\rm core}$, are determined by: $L^{\rm man} = -R_\oplus \cos\theta_z - (R_c^2 - R_\oplus^2 \sin^2\theta_z)^{1/2}$, $L^{\rm core} = 2(R_c^2 - R_\oplus^2 \sin^2\theta_z)^{1/2}$, with $(180^\circ - 33.17^\circ) \leq \theta_z \leq 180^\circ$. Correspondingly, the neutrinos cross the core, the inner core and the outer core for $\cos\theta_z$ lying respectively in the intervals [−1.00, −0.84], [−1.00,−0.98] and [−0.98,−0.84]

In contrast to seismic waves, which are usually reflected or refracted at density jumps, neutrino oscillations are essentially not sensitive to changes of density in the Earth mantle and core taking place over distances which are smaller than the neutrino oscillation length [62] (see also [27]) that in the cases we are going to study is typically ~ 500 km.[2] Thus, they are sensitive, in general, to the average densities of the mantle (or layers of the mantle having width ~ 1000 km), and of the inner core and the outer core (or possibly of two layers of the outer core (mantle) each having width ~ 1000 km). However, through the mantle-core interference (or neutrino oscillation length resonance- (NOLR-) like) effect [64–66] (see also [67–69] and references quoted therein), the neutrino oscillations are sensitive to densities of the mantle and the core as well as to the difference of the densities of the mantle and the core, i.e., to the magnitude of the density "jump" in the mantle-core narrow transition zone. They might be sensitive, in principle, also to the difference between the IC and OC (average) densities.

The Earth matter effects in the neutrino oscillations of interest depend on the matter potential [70–72]

$$V = \sqrt{2}\, G_{\rm F}\, N_e\,, \tag{1}$$

which involves the electron number density N_e along the path of the neutrinos. The relation between the Earth density and electron number density includes the electron fraction number Y_e (or Z/A factor) of the corresponding Earth structure or layer: $N_e^{(E)}(r) = \rho_{\rm E}(r)\, Y_e/m_{\rm N}$, where $m_{\rm N}$ is the nucleon mass. For isotopically symmetric matter $Y_e = 0.5$. However, the compositions of the Earth mantle and core are not exactly isotopically symmetric. For the outer core, for example, different composition models give a value of Y_e in the interval $Y_e^{oc} = 0.466 - 0.471$ (see, e.g., [1,28–31]). The value of Y_e in the mantle is closer to 0.5 [1,10]: $Y_e^{man} = 0.490 - 0.497$. In this study we will use the following default values of Y_e in the mantle and the core: $Y_e^{man} = 0.50$ and $Y_e^{c} = 0.50$. The results we will obtain change insignificantly if instead we used values of Y_e^{oc} and Y_e^{man} from the above quoted intervals.

As is well known, for NO (IO) neutrino mass spectrum, the matter effects can lead to strong enhancement of the neutrino (antineutrino) transition probabilities of interest $P(\nu_l \rightarrow \nu'_l) \equiv P_{ll'}$ and $P(\bar{\nu}_l \rightarrow \bar{\nu}'_l) \equiv \bar{P}_{ll'}$, $l \neq l' = e, \mu$, and $l = e$, $l' = \tau$, for neutrino energies $E \sim (6 - 10)$ GeV and $\sim (3 - 5)$ GeV, corresponding respectively to the resonance in the mantle [70,73] (see also [71]) and to the mantle-core interference (NOLR) effect [64]. In our analysis we consider all neutrino interactions in the energy interval, $E = (1 - 100)$ GeV, well covering the most sensitive range to density dependent effects which are contained in the energy interval $E \sim (2 - 10)$ GeV, and taking into account the effects of the energy resolution.

The neutrino oscillation probabilities are calculated taking into account the variation of densities in inner core, outer core, and the two mantle layers, so that they reproduce the results corresponding to the variations predicted by the PREM model. A more detail discussion is given in Sect. **??**. The neutrino oscillations parameters used as input in the calculations of the probabilities are given in Table 1. At neutrino energies $E_\nu \geq 2$ GeV we will be interested in the effects of Δm^2_{21} and the Dirac CP-violation phase δ in the oscillation probabilities are subleading being strongly suppressed. We do not take into account the uncertainties in the determination of the neutrino oscillation parameters since their effect is much smaller than the effects of the systematic and statistical uncertainties accounted for in the calculations.

---

[2] The estimate we quote refers to the relevant quantity, $L_{\rm osc}/(2\pi)$, $L_{\rm osc}$ being the neutrino oscillation length.

Table 1 PMNS parameters used in the study, $s_{ij}^2 \equiv \sin^2\theta_{ij}$. The values correspond to the best fit point in Ref. [74] for normal neutrino mass ordering

Ordering	s_{13}^2	s_{12}^2	s_{23}^2	δ_{CP}	Δm_{32}^2 (10^{-3} eV^2)	Δm_{21}^2 (10^{-5} eV^2)
Normal	0.022	0.307	0.45	− 1.75	2.40	7.53

2.1 Earth total mass, moment of inertia and hydrostatic equilibrium constraints

In order to estimate the sensitivity of the HK detector to possible deviations of the core (IC + OC) and the two mantle layers densities from those obtained using geophysical and seismological data and described by PREM, in the statistical analysis we have performed we varied the density of each of these structures, as is typically done in the neutrino tomography studies of the Earth interior. We will assume that that the variations and changes of $\rho_{\rm IC}$, $\rho_{\rm OC}$, $\rho_{\rm lman}$ and $\rho_{\rm uman}$ are by constant r-independent factors $\kappa_{\rm IC}$, $\kappa_{\rm OC}$, $\kappa_{\rm lman}$ and $\kappa_{\rm uman}$:

$$\rho_i' = (1+\kappa_i)\,\rho_i\,,\;\; i = \text{IC, OC, lman, uman}\,, \kappa_i > -1\,. \quad (2)$$

In this study we will consider the case of variation of $\rho_{\rm IC}$ and $\rho_{\rm OC}$ by the same factor:

$$\kappa_{IC} = \kappa_{OC} = \kappa_C\,. \quad (3)$$

In our analysis we implemented the constraints on the variations of ρ_{IC}, ρ_{OC}, ρ_{lman} and ρ_{uman} following from the precise knowledge of the Earth mass and moment of inertia: [47,48,75]:

$$M_\oplus = (5.9722 \pm 0.0006)\times 10^{24}\ \text{kg}, \quad (4)$$

$$I_\oplus = (8.01736 \pm 0.00097)\times 10^{37}\ \text{kg m}^2. \quad (5)$$

The mean value of $I_\oplus$ can be related to the Earth mean total mass and radius $R_\oplus$:

$$I_\oplus = C_{\rm G(PREM)}\, M_\oplus\, R_\oplus^2\,. \quad (6)$$

where $C_{\rm G}$ ($C_{\rm PREM}$) is a constant determined in gravity experiments (the PREM model):

$$C_{\rm G} = 0.330745\,, \quad C_{\rm PREM} = 0.33080\,. \quad (7)$$

It is well known from the seismological and geophysical studies that in order for Earth to be in hydrostatic equilibrium the following inequalities should always hold:

$$\rho_{man}' < \rho_{OC}' < \rho_{IC}'\,. \quad (8)$$

In the present analysis we will require that these Earth hydrostatic equilibrium (EHE) conditions are satisfied by the average densities of the corresponding Earth layers, $\bar\rho_i' = \bar\rho_i(1+\kappa_i)$.

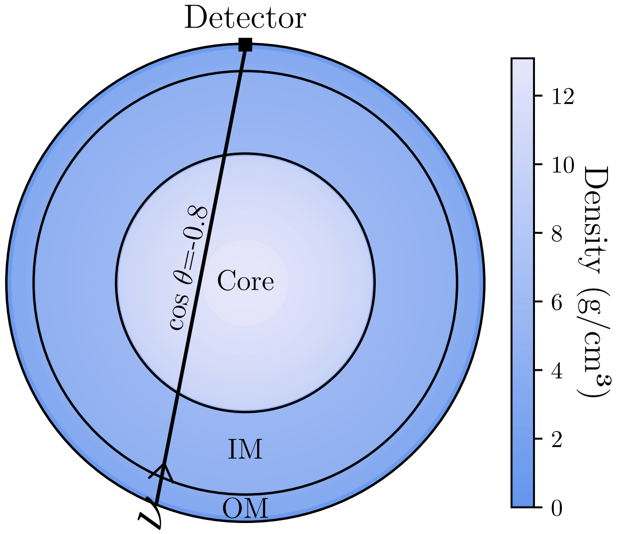

Fig. 1 A diagram of the Earth interior under study. The angle $\cos\theta = -1$ corresponds to an up-going neutrino crossing the Earth along the diameter before being detected

We implement the total Earth mass $M_\oplus$ and moment of inertia $I_\oplus$ constraints by compensating the variation of the density in the structure of interest, for example, ρ_{OC} or ρ_C, by corresponding change of the densities in two other density structures such that the EHE conditions are also satisfied.

It was shown in [63] that if we approximate the Earth density structure with the standard three layers – the inner core, outer core and mantle, the $M_\oplus$, $I_\oplus$ and EHE constraints limit severely the allowed ranges of variations of densities in these layers. For example, κ_{OC} is constrained to lie in the interval $-0.036 \leq \kappa_{OC} < 0.01$. None of the currently operating and planned future detectors can be sensitive to such small deviations of $\bar\rho_{OC}$, $\bar\rho_{IC}$ and $\bar\rho_{man}$ from their respective PREM values.

In our analysis we will use effectively a three-layer model of Earth density distribution consisting in the core and two-lower and upper-mantle layers.[3] The lower mantle layer extends from $R_c = 3480$ km to $R_{\rm lman} = 5701$ km, and has an average density $\bar\rho_{\rm lman} = 4.90$ g/cm^3 , while the upper mantle one extends from $R_{\rm lman} = 5701$ km to $R_{\rm man} = 6371$

---

[3] The same three-layer Earth density structure was used in the study of the DUNE detector potential to perform neutrino tomography of the Earth [54].

km, having an average density $\bar{\rho}_{\rm uman} = 3.60$ g/cm^3. This density structure is shown in Fig. 1.

Since in the case we study the mantle is divided into two layers and $\kappa_{IC} = \kappa_{OC} = \kappa_C$, so that $\bar{\rho}'_{OC} < \bar{\rho}'_{IC}$ is always fulfilled, we consider the following form of the EHE conditions:

$$\bar{\rho}'_{uman} < \bar{\rho}'_{lman} < \bar{\rho}'_C \,. \tag{9}$$

In the specific case we consider with the EHE constraints given in Eq. (9), we implement the $M_\oplus$ and $I_\oplus$ constraints by compensating the variation of the density of the core $\bar{\rho}_C$ by corresponding change of the densities in two mantle layers $\bar{\rho}_{lman}$ and $\bar{\rho}_{uman}$. This is illustrated in the left panel in Fig. 2. A given modification of the PREM density profile of the Earth leads to a corresponding modification of neutrino oscillation probabilities. For the case of the densities shown in the left panel in Fig. 2 we show in the right panel of the same figure the changes of the oscillation probabilities for $\cos\theta_z = -1, -0.8$.

We follow the procedure described in [63]. The values of $M_\oplus$ and $MoI \equiv I_\oplus$ are calculated by integrating the polynomials describing the density distributions in the PREM model. Using the $M_\oplus$ and $I_\oplus$ constraints we can express the constants parametrising the deviations of the lower and upper mantle average densities from their PREM values, κ_{lman} and κ_{uman}. in terms of the constant κ_C parametrising the deviation of the core (outer core) average density. Working with $\bar{\rho}'_{uman}$, $\bar{\rho}'_{lman}$ and $\bar{\rho}'_C$ we find:

$$\kappa_{lman} = f_{lman}\,\kappa_C\,,\;\; f_{lman} = -1.43;\, \kappa_{uman} = f_{uman}\,\kappa_C$$
$$f_{uman} = 2.070\,. \tag{10}$$

We remark that if we use $\bar{\rho}'_{OC}$ instead of $\bar{\rho}'_C$ we obtain somewhat different values of f_{lman} and f_{uman}: $f_{lman} = -1.539$ and $f_{uman} = 2.425$. Thus, in both cases in order to compensate the variation of the density in the core, the density should be increased in one of the mantle layers and decreased in the second mantle layer.

In the case of $\kappa_C < 0$, the relevant EHE constraint in Eq. (9) is $\bar{\rho}_{lman}(1 + \kappa_{lman}) < \bar{\rho}_C(1 + \kappa_C)$. Using the relation between κ_{lman} and κ_C in Eq. (10) and the values of $\bar{\rho}_{lman}$ and $\bar{\rho}_C$, one can show this constraint is satisfied for $\kappa_C > -0.335$. This in turn implies that $\kappa_{lman} < 0.482$ and $\kappa_{uman} > -0.693$. Summarising, in the case of $\kappa_C < 0$, the $M_\oplus$, $I_\oplus$ and the EHE constraints (9) lead to:

$$\kappa_C > -0.335\,,\; \kappa_{lman} < 0.482\,,\; \kappa_{uman} > -0.693\; (\kappa_C < 0)\,. \tag{11}$$

The most stringent constraint on $\kappa_C > 0$ follows from the requirement that when we vary κ_C, and correspondingly κ_{uman} and κ_{lman}, the inequality $\bar{\rho}'_{uman} < \bar{\rho}'_{lman}$ should always hold (Eq. (9)). This condition reads: $\bar{\rho}_{uman}(1 + \kappa_{uman}) < \bar{\rho}_{lman}(1+\kappa_{lman})$. Employing the relations between κ_{uman}, κ_{uman} and κ_C given in Eq. (10) we get:

$$\kappa_C < \frac{\bar{\rho}_{lman} - \bar{\rho}_{uman}}{f_{lman}\bar{\rho}_{lman} + f_{uman}\bar{\rho}_{uman}} \cong 0.089\,, \tag{12}$$

where we have used the numerical values of f_{lman}, $\bar{\rho}_{lman}$, f_{uman} and $\bar{\rho}_{uman}$. This upper limit on $\kappa_C > 0$ in turn implies $\kappa_{uman} < 0.184$ and $\kappa_{lman} > -0.128$.

Combing the results for negative and positive κ_C, which correspond to the EHE constraints in Eq. (9) for the average densities, we have:

$$\begin{aligned} &-0.33 < \kappa_C < 0.09 \\ &-0.13 < \kappa_{lman} < 0.48 \\ &-0.69 < \kappa_{uman} < 0.18\,. \end{aligned} \tag{13}$$

We get similar ranges of allowed values of κ_C, κ_{lman} and κ_{lman} if in the preceding discussion we used $\bar{\rho}'_{OC}$ instead of $\bar{\rho}'_C$. At the same time, using the EHE constraints in Eq. (8) leads to weaker restrictions on κ_C, κ_{lman} and κ_{lman}[4].

We have performed also a numerical scan to determine the values of κ_i, $i = C, lman, uman$, which satisfy the $M_\oplus$, $I_\oplus$ and the EHE constraints. In this scan the conservation of $M_\oplus$ and $I_\oplus$ are required to be fulfilled with a numerical uncertainty of 1% of the nominal values of $M_\oplus$ and $I_\oplus$. The EHE constraint is imposed by requiring that the inequalities in Eq. (9) are always satisfied for the corresponding average densities. Following the described procedure we find:

$$\begin{aligned} &-0.30 < \kappa_C < 0.10 \\ &-0.15 < \kappa_{LMT} < 0.45 \\ &-0.65 < \kappa_{UMT} < 0.10 \end{aligned} \tag{14}$$

The above results obtained numerically we are going to use in what follows agree very well with the results in Eq. (13) derived analytically.

It follows from Eqs. (13) and (14) that the $M_\oplus$, $I_\oplus$ and EHE constraints limit in the case of the three-layer Earth density structure we are considering the possible deviations

---

[4] This case was analised in Ref. [63] with $\bar{\rho}_{IC}$ kept at its PREM value and the mantle divided in upper and lower mantle layers. We note that in the expression of the denominator in the right-hand side of the inequality in Eq. (69) in [63], the signs in the front of the second and third terms should be negative, i.e., the correct form of this expression is: $\bar{\rho}_{OC} - \bar{\rho}_{lman}\,C_{lman}\,f_{lman} - \bar{\rho}_{uman}\,C_{uman}\,f_{uman}$, where f_{lman}, f_{uman} and C_{lman} and C_{uman} are defined in Eqs. (65) and (68), respectively. Correspondingly, the inequality in Eq. (70) changes to $\kappa_c > -0.496$. However, the strongest lower limit in the case of $\kappa_c < 0$ follows from the EHE constraint $\bar{\rho}_{uman}(1+\kappa_{uman}) < \bar{\rho}_{OC}(1+\kappa_{OC})$: $\kappa_c > -0.334$. The strongest upper limit on $\kappa_c > 0$ follows from the EHE condition that $\bar{\rho}_{uman}(1+\kappa_{uman}) < \bar{\rho}_{lman}(1+\kappa_{lman})$: $\kappa_c < 0.086$. Thus, Eq. (71) in [63] should read: $-0.334 < \kappa_c < 0.086$.

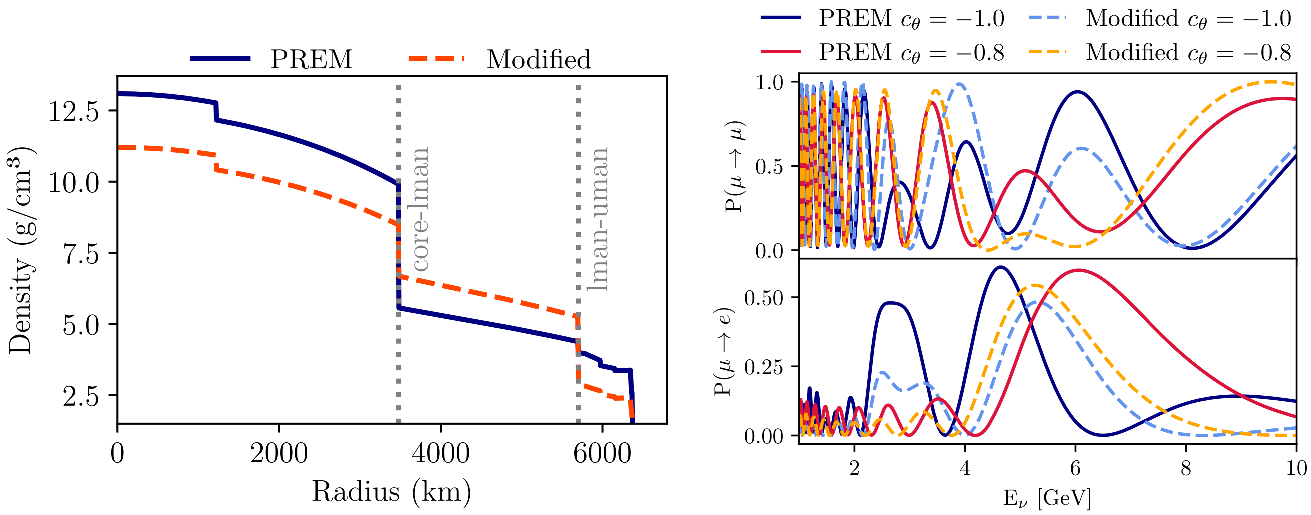

Fig. 2 Left panel: Earth density according to PREM and an example solution for a modified Earth with fixed $\kappa_{lman} = 0.2$. Right panel: ν_ν disappearance and ν_e appearance probabilities for two values of the azimuth angle and the Earth models shown in the left panel

of $\bar{\rho}_C$, $\bar{\rho}_{lman}$ and $\bar{\rho}_{uman}$ from their respective PREM values of 10.99 g/cm^3, 4.90 g/cm^3 and 3.60 g/cm^3 to the following rather narrow intervals: 7.36 g/cm^2 $< \bar{\rho}_C <$ 11.98 g/cm^3, 4.26 g/cm^3 $< \bar{\rho}_{lman} <$ 7.25 g/cm^3 and 1.12 g/cm^3 $< \bar{\rho}_{lman} <$ 4.23 g/cm^3, where [5] we have used the ranges of κ_i given in Eq. (13).

3 Analysis methodology

This study uses the public release [76] of the simulated atmospheric neutrino event rate predictions generated by the Super-Kamiokande (SK) collaboration in its latest atmospheric neutrino oscillation analysis [74]. It includes realistic flux [77], neutrino interaction modeling using NEUT [78,79] detector effects and analysis sample selection criteria, see Sect. 3.2. Based on those simulations, we extrapolate the Earth tomography sensitivity to Hyper-Kamiokande (HK), a detector eight times larger than SK, but based on the same detection concept and with small instrumentation differences. Additionally, we modify the nominal distributions, as later discussed in Sect. 3.6, to assess the potential impact of enhanced energy and/or angular resolutions in HK. The reported sensitivities are obtained as described in Sect. 3.7.

3.1 SK simulation input

Our study utilizes as input the simulation release in Ref. [76]. It consists of the expected event rates, and one-dimensional true energy and angle event distributions for a list of 931 angle and energy bins divided in 29 samples, corresponding to 29 different sets of event selection conditions. The distributions are released as 1D true neutrino energy and true azimuth angle quantiles at 2.3%, 15.9%, 50%, 84.1% and 97.7% of the distribution. The predictions are divided in three major blocks, consisting of the unoscillated, and oscillated predictions assuming either the normal or the inverted mass ordering. For each, the predictions are divided in six components: ν_e, ν_μ, $\bar{\nu}_e$, $\bar{\nu}_\mu$, $\nu_\tau + \bar{\nu}_\tau$ and neutral current (NC). Additionally, the measured data counts in every bin are provided. It is important to note that it is not possible to use data counts as Super-Kamiokande does only release the prefit event rate expectations, namely, without applying the systematic pulls at the best fit point. Therefore, we focus in this study on the analysis of the nominal simulation expectations, which are in any case an excellent proxy to study the sensitivity of future similar experiments.

3.2 Selection samples

The 29 selections samples can be sub-divided in 19 samples without and 10 with neutron tagging, often indicated with additional labels 0 n, 1 n, etc. This large number of samples is the result, in part, to splitting some samples in two phases of the Super-Kamiokande experiment, i.e. data from SK runs 1 to 3 and from runs 4 to 5, further details on the specifics of this data periods are available in Ref. [74]. As we are primarily interested in Hyper-Kamiokande, whenever this

---

[5] Similar restrictions were obtained in Ref. [54]. Numerically, our results differ somewhat from those found in [54] since in the constraint following from the conservation of $I_\oplus$ the authors used the average densities of the considered three density layers present in the expression for $M_\oplus$ (Eqs. (5.3) and (5.4) in [54]), while, we have utilised the results of the analysis in [63] which showed that the average densities in the expression for $I_\oplus$ differ somewhat form those in the expression for $M_\oplus$.

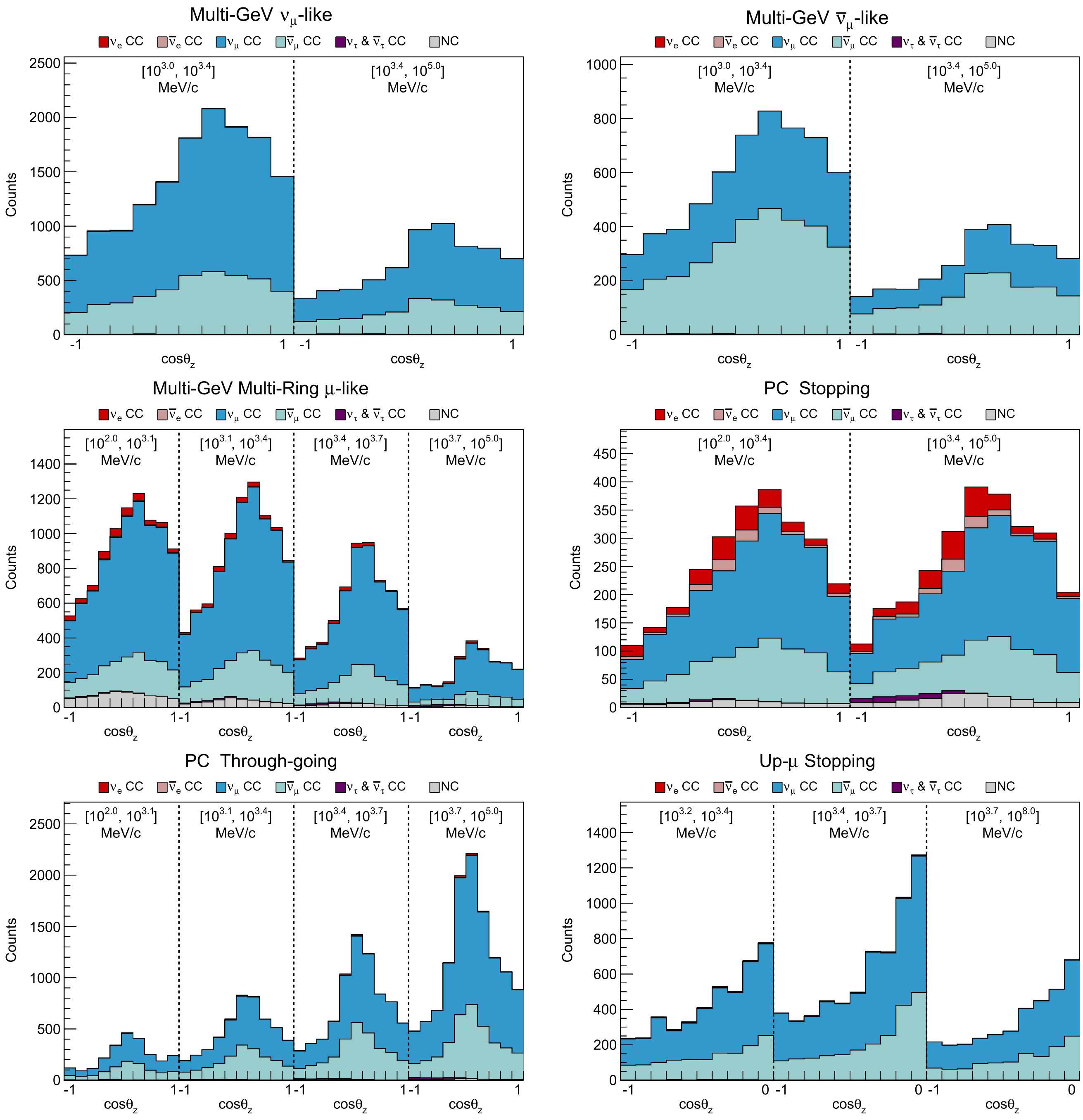

Fig. 3 Oscillated predictions, using parameters in Table 1, for muon-rich samples scaled to 6500-live days and considering a ×8 increased mass to scale Super-Kamiokande to Hyper-Kamiokande. All 2D distributions are presented in reconstructed lepton momentum slices

duplicity exist we use the performances of the simulations for runs 4 and 5.

Broadly speaking there are 4 different categories of samples: Sub-GeV samples, Multi-GeV samples, NC-samples, and non-fully-contained (non-FC) samples. Oscillations of neutrinos with energy below 1 GeV change very rapidly with energy and azimuth angle, see previous Fig. 2, such that tomography-sensitive variations get largely averaged out. Therefore we do not consider Sub-GeV samples. Similarly, as our interest regards effects in the neutrino flux flavor composition, we do not include NC-samples, insensitive to flavor transitions. Lastly, we only consider those samples that have a significant fraction of events with energies of interest. Accordingly, we ignore the Up-μ showering and Up-μ stopping samples, which largely consist of events with energies above several tens of GeV.

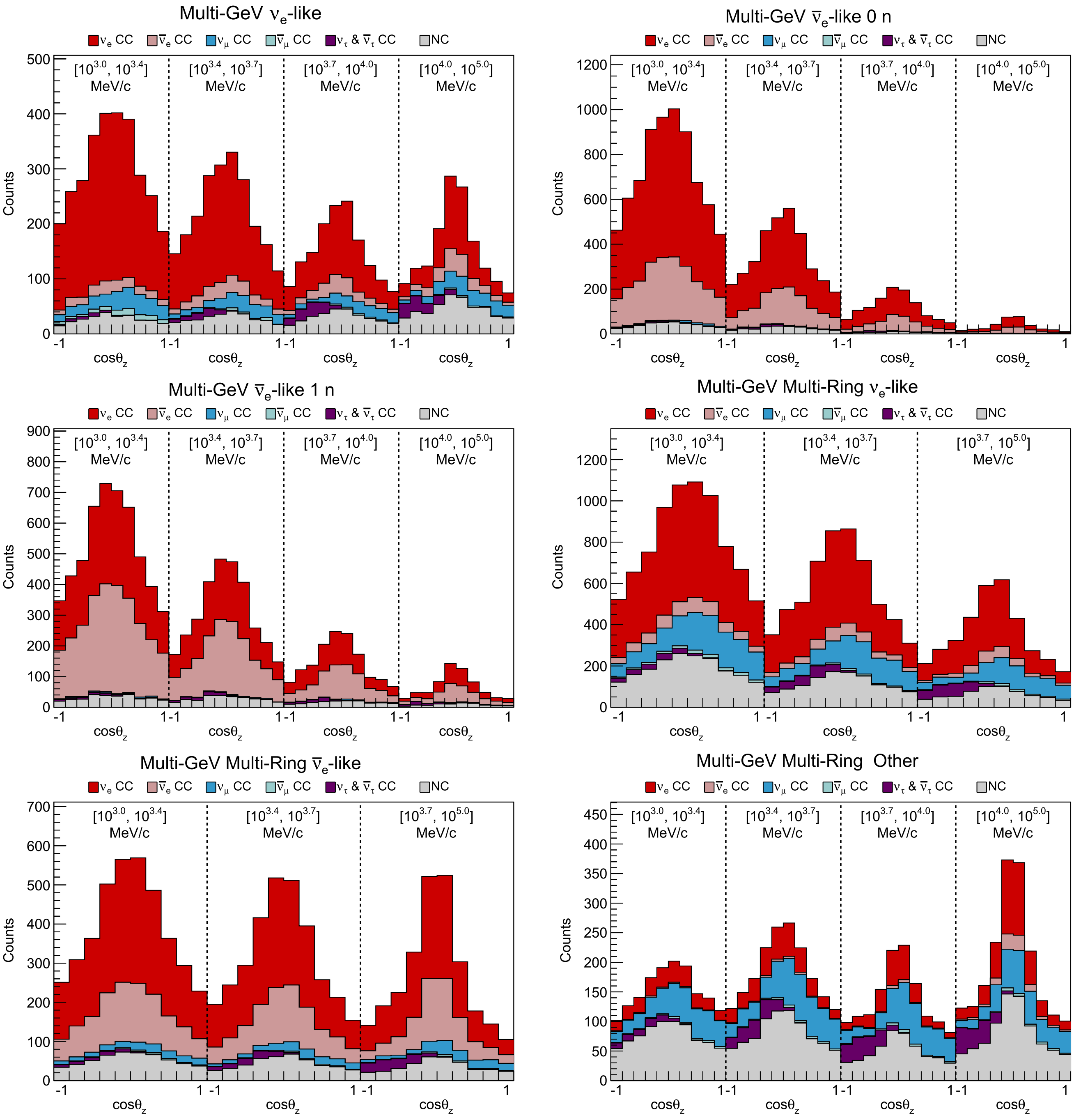

Fig. 4 Oscillated predictions, using parameters in Table 1, for electron-rich samples scaled to 6500-live days and considering a ×8 increased mass to scale Super-Kamiokande to Hyper-Kamiokande. All 2D distributions are presented in reconstructed lepton momentum slices

Therefore, in this analysis we utilize a total of 12 selection samples, consisting of Multi-GeV events with a single lepton ring (ν_μ, $\bar{\nu}_\mu$, ν_e, $\bar{\nu}_e$ 0 n, $\bar{\nu}_e$ 1 n) and Multi-GeV events with multiple rings (ν_μ, ν_e, $\bar{\nu}_e$ and other), and non-FC events (partially contained stopping, partially contained through-going and Up-μ stopping). All the analysis samples under consideration are presented in Figs. 3 and 4.

3.3 Neutrino fluxes

We use the same neutrino flux used by the Super-Kamiokande collaboration to generate its expected event counts, namely we utilize the flux prediction of Honda et al. [77]. In the unoscillated prediction, a tiny flux of $\nu_\tau + \bar{\nu}_\tau$ is expected. If one would run this nominal expectation through Super-Kamiokande's event production and analysis pipeline, only a very small statistical sample of $\nu_\tau + \bar{\nu}_\tau$ would be obtained, making it difficult to evaluate through simulations the reconstruction and selection performances and efficiencies in each sample for this flavor. To solve this in a simple manner, the Super-Kamiokande collaboration calculates the expected $\nu_\tau + \bar{\nu}_\tau$ event rate using for it Honda et. al. model's ν_μ flux, and later down-scales the events to their appropriate value. We take this method into account in our calculations.

3.4 Oscillation probability evaluation

The three-flavour oscillation probability is evaluated using the `Prob3++` framework,[6] developed by Super-Kamiokande collaborators. The framework calculates the oscillation probability including matter effects for any neutrino flavor transition as a function of the input PMNS parameters, the values of the neutrino mass squared differences values, and the Earth model configuration, which is input as a collection of density values along the Earth radius. `Prob3++` takes as input the Earth density profile given by a collection of points. We evaluate the Earth density at 82 points along the Earth radius. A subset of 61 points are distributed from 0 to 5600 km every 100 km, with few additional points near the shell transitions. The remaining points describe the 5600–6371 km region, sampled more frequently at irregular intervals to reflect the finer structure of the Earth crust.

The oscillation probability is calculated in every bin i and for every neutrino flavour α. The oscillated and nominal expected number of counts for the α flavor in the i-th bin, $N^{osc}_{i,\alpha}$ and $N^{nominal}_{i,\alpha}$, are related as follows:

$$N^{osc}_{i,\alpha} = N^{nominal}_{i,\alpha} \times \Phi^{osc}_{i,\alpha} / \Phi^{nominal}_{i,\alpha}, \tag{15}$$

where $\Phi^{osc}_{i,\alpha}$ and $\Phi^{nominal}_{i,\alpha}$ represent the oscillated and nominal fluxes of ν_α in the i-th bin. To calculate the nominal flux, we evaluate the Honda flux model for the α flavor at the average neutrino energy and average zenith angle for the charged-current events associated to that flavor in the bin.

Event-by-event reweighting for neutrino oscillation effect is implemented in SK. However, the data and simulation releases consist of a simpler representation that loses the event-by-event details. Therefore, we instead conduct a quantile-weighted evaluation of the oscillation probability in every bin. Example spline distributions are presented in Fig. 5.

The procedure is as follows:

- We use Piecewise Cubic Hermite Interpolating Polynomial (PHCIP) [80] monotonic splines to interpolate the quantiles.
- We define a number of equally spaced points, $N_q \in [0, 1]$, forming a homogeneously spaced $N_q \times N_q$ grid. For every bin then we calculate the probability as a weighted sum:

$$\Phi^{osc}_{i,\alpha} = \Phi_\alpha \times \left(\sum_i^{N_q} \sum_j^{N_q} w_i \times w_j \times P^{\alpha\to\alpha}_{osc}(E_i, \theta_j) \right) + \sum_{\beta\neq\alpha} \Phi_\beta \times \left(\sum_i^{N_q} \sum_j^{N_q} w_i \times w_j \times P^{\beta\to\alpha}_{osc}(E_i, \theta_j) \right), \tag{16}$$

  where w_i, w_j denote the width of the interval between two quantile points, with associated energy and azimuth angle values E_i and θ_j evaluated at the center of that interval, $P^{\beta\to\alpha}_{osc}(E_i, \theta_j)$ and $P^{\alpha\to\alpha}_{osc}(E_i, \theta_j)$ being respectively the $\nu_\beta \to \nu_\alpha$ transition and the ν_α survival oscillation probabilities.

For increasing N_q the quantile intervals become smaller, closely reproducing the energy and angle distributions and ensuring a small variation of the oscillation probability from point to point. We use $N_q = 15$ as we observed that finner grid sizes had no observable impact on the results.

3.5 Analysis datasets

We explore several scenarios for different assumptions of systematic uncertainties. In all cases we consider the same PID capabilities as in SK.

First, we consider the expected sensitivity for SK `SK-Nominal`, directly utilizing SK distributions and expected bin counts as in [74] for the sub-set of samples considered in this work. Similarly, we report expected sensitivities scaled to HK's effective detection volume and 6500 days of data (HK-Nominal), the same as in Ref. [74].

Second, we consider the expected sensitivity for sets of fake data informed by SK's performances. In total we consider the following detector performances:

1) $\mathrm{E}_{0\%}$ & 10° **2)** $\mathrm{E}_{0\%}$ & 20°; **3)** $\mathrm{E}_{30\%}$ & 0° **4)** $\mathrm{E}_{30\%}$ & 10° **5)** $\mathrm{E}_{20\%}$ & 10° **6)** $\mathrm{E}_{10\%}$ & 10° **7)** $\mathrm{E}_{30\%}$ & 20°.

The notation $\mathrm{E}_{X\%}$ & Y° indicates a E_ν resolution of X% and a neutrino zenith angle resolution of Y°.

Lastly we consider a special case: $\mathrm{E}_{0\%}$ & 0°, an upper bound for the sensitivity given only by statistical uncertainty. We refer to it as *Stats.*.

3.6 Enhanced datasets generation

To generate the alternative datasets with enhanced detector performances, we sample individual events for every flavor ($\nu_e, \nu_\mu, \bar{\nu}_e, \bar{\nu}_\mu, \nu_\tau + \bar{\nu}_\tau$ and NC) from the PCHIP interpolated

---

[6] For details see https://github.com/rogerwendell/Prob3plusplus.

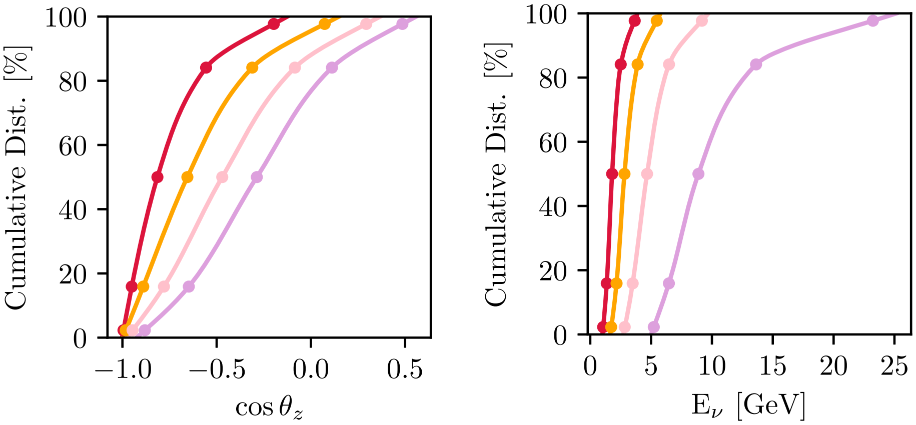

Fig. 5 Example splines in four consecutive energy bins (right panel) and four consecutive angle bins (left panel) in the Multi-GeV Multi-Ring μ-like sample for the ν_μ reaction

true energy and angle quantiles, thus producing un-binned distributions. In total, 10k events are sampled from every true energy and zenith angle bin of every sample. Each event weight corresponds to the number of counts in its original bin normalized by the number of event samples (10k). The reconstructed energy and azimuth angle for each event is then calculated applying a Gaussian smearing to its true simulated energy and azimuth angle according to the assumed detector performances, and events are organized in energy and angle bins accordingly. The resulting predictions are used to calculate 1D true neutrino energy and zenith angle quantile distributions in every reconstructed bin, and are used to generate a new 'fake release' following the very same format as that in Ref. [76]. This allows to run the same analysis pipeline both or SK/HK-Nominal distributions and for the enhanced datasets. To profit from the increase in statistics and the improved detector performances, the enhanced datasets utilize a different binning scheme. In particular, we double the number of angular bins at regular intervals from $\cos\theta = -1$ to $\cos\theta = 0$, and more finely segment the energy bins from 1 to 10 GeV/c. We ignore all bins with $\cos\theta > 0$, corresponding to neutrinos that arrive to the detector from the sky, i.e. without crossing the Earth. The total number of bins for the samples under study gets increased from 390 to 903.

3.7 Sensitivity calculation

The sensitivity to the parameters of interest (κ_C, κ_{lman}, κ_{uman}) is calculated evaluating the statistical consistency of the PREM model expectations with the predictions for a modified Earth according to those parameters, utilizing a fixed choice of PMNS parameters, summarized in Table 1. Specifically, we calculate the $\Delta\chi^2 = \sum_i (O_i - E_i)^2/E_i)$, with E_i and O_i corresponding to the expected PREM model event counts in the bin $i - th$, and O_i corresponding to the expected observed events counts for a modified Earth model in that same bin. We report results for three values of $\sin^2\theta_{23} = 0.45$, 0.50 and 0.58, which essentially span the 3σ allowed range of values of $\sin^2\theta_{23}$ obtained in the latest global analysis of the neutrino oscillation data [81].

4 Results

The sensitivity results for NO neutrino mass spectrum are presented in Fig. 6. Firstly, we note that the sensitivity of a detector with energy and zenith angle resolutions $E_{30\%}$ & 20° in all samples is similar to the HK-Nominal sensitivity directly extrapolated from the performances of Super-Kamiokande. Correspondingly, we will refer to the case of $E_{30\%}$ & 20° further in the text as "nominal". From that starting point, we can notice that progressive improvements in the energy and angular resolutions would have a strong impact for a tomography of the Earth increasing the sensitivity to possible deviations from the PREM density values. Our results suggest that enhancing the angular resolution would translate more directly in tomography sensitivity enhancement. For instance, the resolutions $E_{30\%}$ & 10° and $E_{0\%}$ & 20° provide very similar sensitivities, while for $E_{30\%}$ & 0° the sensitivity is much better. In the case of having a better angular resolution, further improvement of the energy reconstruction would of course have a positive impact, as evidenced by the sensitivity in the $E_{20\%}$ & 10° and $E_{10\%}$ & 10° cases. Even in those scenarios, a notable margin to reach the ultimate sensitivity, given by the statistical only uncertainty case, exists – indicating that the measurement sensitivity is dominated by systematic uncertainties, as follows by comparing the results corresponding to $E_{0\%}$ & 10° and HK *Stats*. An illustration of the extreme regimes of what is expected to be achieved and what could be best achieved in Hyper-Kamiokande is presented in Fig. 7. We show results for $\sin^2\theta_{23} = 0.45$, 0.50 and 0.58. The three values essentially span the 3σ allowed range of values of $\sin^2\theta_{23}$ obtained in the most recent global analysis of neutrino oscillation data [81]. While comparing the results it is easy to notice that the true value of $\sin^2\theta_{23}$ has a significant impact on the HK sensitivity.

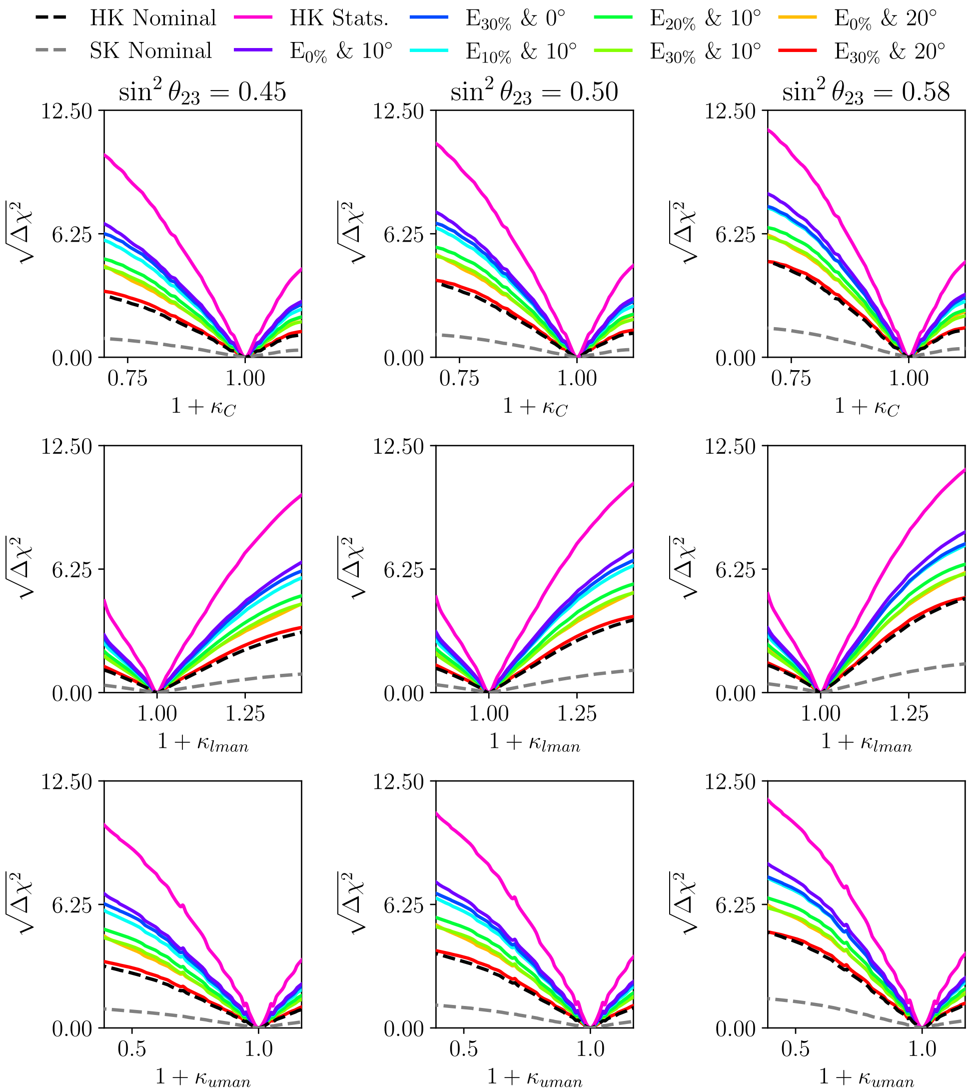

Fig. 6 Sensitivity to deviations of the Earth core, lower mantle and upper mantle densities from their respective PREM values, parametrised as $\rho_i(1+\kappa_i)$, $i = c, lman, uman$, ρ_i being the PREM densities, for different HK detector configurations. The left, center and right columns correspond to: $\sin^2\theta_{23} = 0.45$, 0.50 and 0.58

We summarise our results on the sensitivity of the HK experiment to possible deviations of the core, lower mantle and upper mantle average densities from their respective PREM values in Table 2.

We find, in particular, that for $\sin^2\theta_{23}$ and the "nominal" energy and zenith angle resolutions of E$_{30\%}$ & 20° in all samples, after 6500 days of operation the HK experiment can determine the Earth core average density at 2σ C.L. with a relative uncertainty $\Delta\bar{\rho}_C/\bar{\rho}_C = 100\%\kappa_C$ of (-14.5%)/+39.5 $(-0.145 \leq \kappa_c \leq 0.395)$. For $\sin^2\theta_{23} = 0.58$ the uncertainty is noticeably smaller: (-9.3%)/+31.7% $(-0.093 \leq \kappa_c \leq 0.317)$. However, as we have shown, the $M_\oplus$, $I_\oplus$ and EHE constraints limit the possible maximal deviation of $\bar{\rho}_C$ from its PREM value to 10% ($\kappa_c < 0.10$, see Eqs. (13) and (14)).

The sensitivity of the HK experiment will be much higher in the case of energy and angular resolutions of E$_{20\%}$ & 10°. It increases also significantly with $\sin^2\theta_{23}$. Indeed, in this case at 2σ CL we have for $\sin^2\theta_{23} = 0.45$, 0.50 and 0.58, respectively: (-9.2%)/+11.3% $(-0.092 \leq \kappa_c \leq 0.113)$, (-8.3%)/+9.8% $(-0.083 \leq \kappa_c \leq 0.098)$ and (-6.7%)/+8.5% $(-0.067 \leq \kappa_c \leq 0.085)$. Thus, if, e.g., $\sin^2\theta_{23} = 0.50$, the HK experiment would be able to establish that the average core density at 2σ CL lies in the rather narrow interval: 10.08 g/cm^3 $\leq \bar{\rho}_C \leq 12.06$ g/cm^3, with the PREM value of $\bar{\rho}_C = 10.99$ g/cm^3. Similarly, it will follow from the HK data that at 2σ CL the average lower and upper mantle densities, have values in the intervals: 4.49 g/cm^3 $\leq \bar{\rho}_{lman} \leq 5.38$ g/cm^3, 3.00 g/cm^3 $\leq \bar{\rho}_{uman} \leq 4.25$ g/cm^3, where we have used the corresponding results in Table 2 and the upper limit $\kappa_{uman} \leq 0.18$ (see Eq. (13)). We recall that the PREM values of $\bar{\rho}_{lman}$ and $\bar{\rho}_{uman}$ are 4.90 g/cm^3 and 3.60 g/cm^3, respectively.

Given the PREM values of $\bar{\rho}_{man} = 4.66$ g/cm^3 and $\bar{\rho}_{IC} = 12.89$ g/cm^3, the HK result on $\bar{\rho}_C$ would be an independent confirmation of the existence of at least three major density layers in the interior of the Earth.

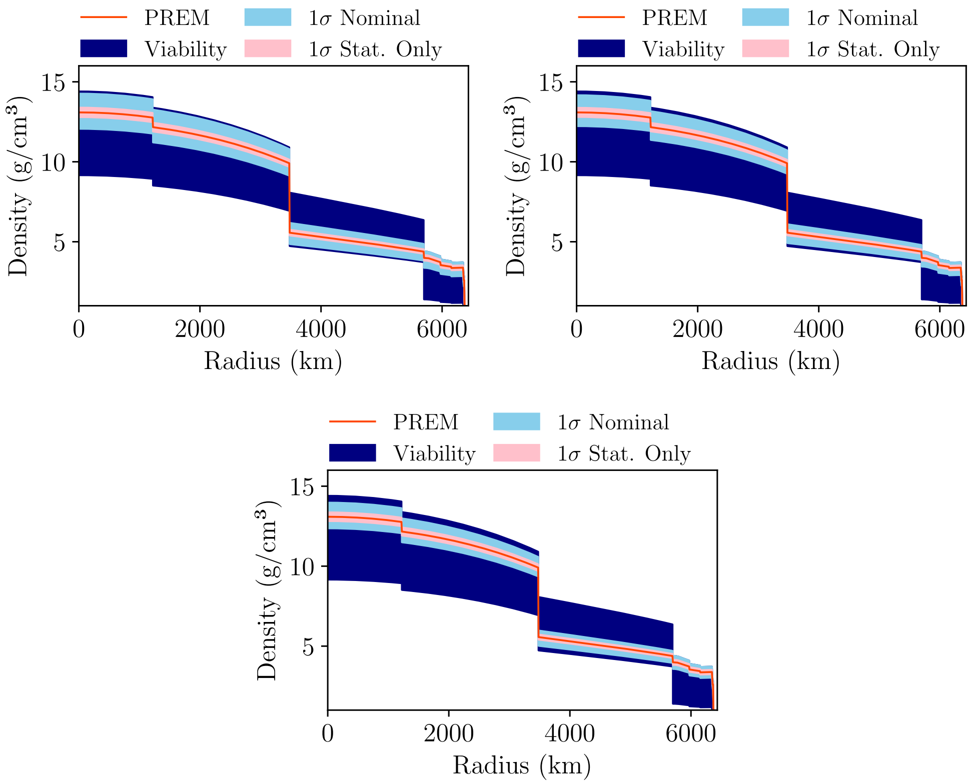

Fig. 7 Confidence intervals of HK sensitivity to deviations of the core, lower mantle and upper mantle average densities from their respective PREM values. The dark blue bands correspond to varying κ_C in the interval $-0.30 < \kappa_C < 0.10$, allowed by the Earth total mass, moment of inertia and hydrostatic equilibrium constraints (see Eq. (14)). The light blue and red bands represent the 1σ Nominal and Stats. Only confidence level intervals. The top left, top right and bottom panels correspond respectively to $\sin^2\theta_{23} = 0.45$, 0.50, 0.58. See text for further details

Table 2 The 68% and 95% CL intervals of sensitivity of the HK experiment to the parameters $(1+\kappa_C)$, $(1+\kappa_{lman})$ and $(1+\kappa_{uman})$, characterising the deviations of the inner and outer core, lower mantle and upper mantle densities from their respective PREM values, for different sets of HK energy and angular resolutions and $\sin^2\theta_{23} = 0.45$, 0.50 and 0.58. Dashes indicate the limits obtained from the Earth $M_\oplus$, $I_\oplus$ and EHE constraints quoted in Eq. (14) in the cases when they are more constraining than those derived from the analysis of the HK prospective data. See text for further details

	$\sin^2\theta_{23}$	Core (C)				Lower mantle				Upper mantle			
		68%		95%		68%		95%		68%		95%	
Model		Lower	Upper	Lower	Upper	Lower	Upper	Lower	Upper	Lower	Upper	Lower	Upper
HK nominal	0.45	0.922	1.090	0.834	–	0.873	1.111	–	1.228	0.844	1.184	0.671	–
	0.50	0.934	1.082	0.867	–	0.883	1.095	–	1.185	0.863	1.168	0.734	–
	0.58	0.945	1.067	0.899	–	0.902	1.074	–	1.145	0.895	1.141	0.793	–
SK nominal	0.45	–	–	–	–	–	–	–	–	–	–	–	–
	0.50	0.762	–	–	–	–	1.333	–	–	0.527	–	–	–
	0.58	0.829	–	–	–	–	1.237	–	–	0.658	–	–	–
HK Stats.	0.45	0.978	1.023	0.953	1.048	0.969	1.033	0.934	1.064	0.958	1.043	0.906	1.096
	0.50	0.978	1.022	0.956	1.046	0.970	1.031	0.937	1.060	0.959	1.042	0.913	1.091
	0.58	0.979	1.021	0.959	1.043	0.972	1.029	0.940	1.056	0.960	1.041	0.922	1.084
$E_{0\%}$ & 10°	0.45	0.963	1.038	0.930	1.075	0.950	1.049	0.894	1.102	0.932	1.069	0.854	1.150
	0.50	0.965	1.036	0.936	1.069	0.954	1.045	0.900	1.092	0.935	1.066	0.868	1.144
	0.58	0.969	1.033	0.942	1.064	0.960	1.041	0.910	1.078	0.939	1.063	0.890	1.129
$E_{30\%}$ & 0°	0.45	0.961	1.040	0.924	1.079	0.945	1.053	0.888	1.108	0.927	1.075	0.848	1.159
	0.50	0.963	1.038	0.932	1.074	0.950	1.048	0.895	1.099	0.933	1.069	0.857	1.149
	0.58	0.966	1.035	0.939	1.066	0.956	1.043	0.904	1.084	0.937	1.065	0.880	1.139

Table 2 continued

	$\sin^2\theta_{23}$	Core (C)				Lower mantle				Upper mantle			
		68%		95%		68%		95%		68%		95%	
Model		Lower	Upper	Lower	Upper	Lower	Upper	Lower	Upper	Lower	Upper	Lower	Upper
$E_{10\%}$ & 10°	0.45	0.959	1.043	0.919	1.086	0.941	1.056	0.877	1.114	0.922	1.083	0.839	1.179
	0.50	0.963	1.040	0.930	1.080	0.946	1.050	0.886	1.102	0.931	1.073	0.854	1.162
	0.58	0.966	1.036	0.939	1.070	0.954	1.043	0.898	1.085	0.937	1.066	0.880	1.145
$E_{20\%}$ & 10°	0.45	0.952	1.051	0.908	1.113	0.930	1.066	0.855	1.135	0.904	1.101	0.803	–
	0.50	0.957	1.046	0.917	1.098	0.937	1.058	0.864	1.117	0.918	1.092	0.833	–
	0.58	0.963	1.040	0.933	1.085	0.945	1.049	0.879	1.098	0.933	1.075	0.859	1.175
$E_{30\%}$ & 10°	0.45	0.945	1.059	0.894	–	0.921	1.074	–	1.150	0.895	1.112	0.788	–
	0.50	0.953	1.054	0.909	–	0.928	1.065	–	1.131	0.905	1.104	0.808	–
	0.58	0.960	1.045	0.924	1.106	0.937	1.054	0.859	1.107	0.926	1.091	0.849	–
$E_{0\%}$ & 20°	0.45	0.949	1.052	0.896	1.116	0.929	1.070	0.854	1.148	0.899	1.102	0.790	–
	0.50	0.955	1.048	0.911	1.104	0.934	1.062	0.860	1.129	0.910	1.096	0.813	–
	0.58	0.961	1.042	0.926	1.090	0.942	1.052	0.871	1.105	0.929	1.081	0.851	1.185
$E_{30\%}$ & 20°	0.45	0.931	1.079	0.855	–	0.889	1.100	–	1.202	0.856	1.157	0.711	–
	0.50	0.939	1.072	0.880	–	0.897	1.085	–	1.169	0.879	1.147	0.760	–
	0.58	0.950	1.063	0.907	–	0.911	1.068	–	1.136	0.900	1.128	0.802	–

5 Conclusions

In the present study we have investigated the potential of the Hyper-Kamikande experiment to perform neutrino tomography of the Earth density structure. Using PREM as a reference model for the Earth density distribution we studied the sensitivity of the Hyper-Kamiokande detector to deviations of the Earth total core average density $\bar{\rho}_C$, lower mantle average density ρ_{lman}, and upper mantle average density, $\bar{\rho}_{uman}$, from their respective PREM values. The analysis is performed by studying the effects of the Earth matter on the oscillations of atmospheric ν_μ, ν_e, $\bar{\nu}_\mu$ and $\bar{\nu}_e$. We used the public release [76] of the simulated atmospheric neutrino event rate predictions generated by the Super-Kamiokande (SK) collaboration in its latest atmospheric neutrino oscillation analysis [74], which includes (i) realistic atmospheric neutrino flux and neutrino interaction modeling, (ii) detector effects, and (iii) analysis of the sample selection criteria. Based on those simulations, we extrapolated the Earth tomography sensitivity to Hyper-Kamiokande (HK), a detector eight times larger than SK, but based on the same detection concept and with small instrumentation differences. Additionally, we modified the nominal distributions (as discussed in Sect. 3.6) to assess the potential impact of enhanced energy and/or angular resolutions in HK.

In investigating the potential of the HK experiment in doing a tomography of the Earth we have considered 6500 days of data, the same as in the latest study by Super-Kamiokande [82]. A significant gap is observed between the Nominal (or "nominal") sensitivity and the sensitivities achieved when using an improved angular and energy resolution (Fig. 7). Therefore, reconstruction improvements from SK to HK, rooted for instance in machine learning techniques, can have a significant impact on the prospects of the HK experiment when performing a neutrino tomography of the Earth.

In our analysis we implemented the constraints on the variations of ρ_C, ρ_{lman} and ρ_{uman} following from the precise knowledge of the Earth mass $M_\oplus$ and moment of inertia $I_\oplus$, as well as from the requirement that the Earth be in hydrostatic equilibrium (EHE).

Considering the case of normal ordering (NO) of neutrino masses, we obtained results which illustrate the dependence of sensitivity to the core, lower and upper mantle densities on the energy and zenith angle resolutions, on whether or not the prospective systematic errors are accounted for and on the value of the atmospheric neutrino mixing angle θ_{23} (Fig. 6, Table 2). We have shown, in particular, that a progressive improvement of the "nominal" energy and angular resolutions of $E_{30\%}$ & 20° of the HK detector would have a strong impact on the Earth tomography potential of the HK experiment. Our results suggest that enhancing the angular resolution has a particularly strong impact increasing the sensitivity of the HK experiment to possible deviations of the considered Earth layers average densities from their respective PREM values.

Performing the analysis for three values of $\sin^2\theta_{23} = 0.45$, 0.50 and 0.58, which essentially span the 3σ allowed range of values of $\sin^2\theta_{23}$ obtained in the latest global analysis of the neutrino oscillation data, we have shown also that the Earth tomography potential of the HK experiment depends strongly on the value of $\sin^2\theta_{23}$.

More specifically, in the case of the "nominal" $E_{res} = 30\%$, $\theta_{zres} = 20°$ and, e.g., $\sin^2\theta_{23} = 0.45$ (0.58), the Hyper-Kamiokande can determine the average core density $\bar{\rho}_C$ at 2σ CL after 6500 days of operation with an the uncertainty of $(-14.5\%)/+39.5\%$ $((-9.3\%/+31/7\%)$, while the $M_\oplus$, $I_\oplus$ and EHE constraints allow in the case of the three layer Earth density structure considered by us a maximal increase of $\bar{\rho}_C$ with respect to its PREM value of less than $\sim 10\%$. In the "more favorable" case of implemented constraints, neutrino energy resolution E_{res} of 20%, zenith angle resolution θ_{zres} of 10% and $\sin^2\theta_{23} = 0.58$ (0.45), the HK experiment can determine the average core density $\bar{\rho}_C$ at 2σ C.L. with an uncertainty of $(-8.3\%)/+9.8\%$ (of $(-9.2\%)/+11.3\%$). If, e.g., $\sin^2\theta_{23} = 0.50$, the HK experiment would be able to establish, in particular, that the average core density at 2σ CL lies in the rather narrow interval: $10.08\ \mathrm{g/cm^3} \leq \bar{\rho}_C \leq 12.06\ \mathrm{g/cm^3}$, with the PREM value of $\bar{\rho}_C = 10.99\ \mathrm{g/cm^3}$. Given the PREM values of the average densities of the mantle and the inner core, $\bar{\rho}_{man} = 4.66\ \mathrm{g/cm^3}$ and $\bar{\rho}_{IC} = 12.89\ \mathrm{g/cm^3}$, this result would be an independent evidence of the existence of at least three major density layers in the interior of the Earth and of the relatively large jump of density in the mantle-core narrow transition zone.

Our results show that the Hyper-Kamiokande experiment, after collecting a sufficiently large data sample, can make a major contribution to the tomography studies of the Earth interior with neutrinos.

Acknowledgements We would like to note that the present study is not a study performed by the Hyper-Kamioknade collaboration although in it we discuss one specific physics problem—that of getting information about the Earth density structure—which can be addressed by the Hyper-Kamioknade experiment. The authors are indebted to Thomas Wester for clarifications on the assumptions and formatting of the Super-Kamiokande's data release. C.J.V. was supported in part by JSPS KAKENHI Grant-in-Aid JP24K17065. The work of S.T.P. was supported in part by the European Union's Horizon 2020 research and innovation programme under the Marie Sklodowska-Curie Grant agreement No. 860881-HIDDeN, by the INFN program on Theoretical Astroparticle Physics and by the World Premier International Research Center Initiative (WPI Initiative, MEXT), Japan. S.T.P would like to thank Kavli IPMU, University of Tokyo, where a major part of this study was done, for the kind hospitality. J.X was supported by Grant-in-Aid for JSPS Fellows P22333.

Data Availability Statement This manuscript has no associated data. [Authors' comment: The only data used in the study corresponds to publicly available data sets from the Super-Kamiokande collaboration cited in the article in ref [76].]

Code Availability Statement Code/software will be made available on reasonable request. [Author's comment: The code/software generated during and/or analysed during the current study is available from the corresponding author on reasonable request.]

Funded by SCOAP^3.

References

1. W.F. McDonough, *Treatise on Geochemistry: The Mantle and Core* ed. by R. W. Carlson, vol. 2 (Elsevier-Pergamon, Oxford, 2003), p. 547
2. B.A. Bolt, Q. J. R. Astron. Soc. **32**, 367 (1991)
3. B.L.N. Kennett, Geophys. J. Int. **132**, 374 (1998)
4. G. Masters, D. Gubbins, Phys. Earth Planet Int. **140**, 159 (2003)
5. F. Nimmo, talk given at the International Workshop "Multi-Messenger Tomography of the Earth", Snowbird, Utah, U.S.A., July 30–31 (2022)
6. K.D. Koper, talk given at the International Workshop "Multi-Messenger Tomography of the Earth", Snowbird, Utah, U.S.A., July 30–31 (2022)
7. L. Waszek, talk given at the International Workshop "Multi-Messenger Tomography of the Earth", APC, Paris, July 4–7 (2023)
8. W.F. McDonough, talk given at the International Workshop "Multi-Messenger Tomography of the Earth", APC, Paris, July 4–7 (2023)
9. S. Noe, talk given at the International Workshop "Multi-Messenger Tomography of the Earth", APC, Paris, July 4–7 (2023)
10. A.M. Dziewonski, D.L. Anderson, Phys. Earth Planet Interiors **25**, 297 (1981)
11. C.F. Yoder, "Global Earth Physics", ed. by T. J. Ahrens, vol. 1 (American Geophysical Union, Washington DC, 1995), p. 1
12. W.F. McDonough, R. Arevalo, J. Phys. Conf. Ser. **136**, 022006 (2008). https://doi.org/10.1088/1742-6596/136/2/022006
13. A. Placci, E. Zavattini, On the possibility of using high-energy neutrinos to study the Earth's interior. https://cds.cern.ch/record/2258764, CERN Report (1973)
14. L.V. Volkova, G.T. Zatsepin, Izv. Akad. Nauk Ser. Fiz. **38N5** 1060 (1974)
15. I.P. Nedyalkov, preprint JINR (Dubna), JINR-P2-81-645 (1981)
16. I.P. Nedyalkov, Bolg. Akad. Nauk **34**, 177 (1981)
17. A. De Rujula, S.L. Glashow, R.R. Wilson, G. Charpak, Phys. Rep. **99**, 341 (1983)
18. T.L. Wilson, Nature **309**, 38 (1984)
19. G.A. Askar'yan, Usp. Fiz. Nauk **144** 523 (1984) [Sov. Phys. Usp. **27** (1984) 896]
20. A.B. Borisov, B.A. Dolgoshein, A.N. Kalinovsky, Yad. Fiz. **44**, 681 (1986)
21. A.B. Borisov, B.A. Dolgoshein, Phys. Atom. Nucl. **56**, 755 (1993)
22. W. Winter, Earth Moon Planets **99**, 285 (2006)
23. C. Kuo et al., Earth Plan. Sci. Lett. **133**, 95 (1995)
24. P. Jain, J.P. Ralston, G.M. Frichter, Astropart. Phys. **12**, 193 (1999)
25. M.M. Reynoso, O.A. Sampayo, Astropart. Phys. **21**, 315 (2004)
26. M.C. Gonzalez-Garcia, F. Halzen, M. Maltoni, H.K.M. Tanaka, Phys. Rev. Lett. **100**, 061802 (2008). [arXiv:0711.0745 [hep-ph]]
27. M. Tanabashi et al., [Particle Data Group], Phys. Rev. D **98** 030001 (2018). https://doi.org/10.1103/PhysRevD.98.030001. See therein

the review “Neutrino Masses, Mixing and Oscillations” by K. Nakamura and S.T. Petcov
28. J. Badro et al., Proc. Natl. Acad. Sci. USA **112**(40), 12310–12314 (2015)
29. E. Kaminski, M. Javoy, Earth Planet. Sci. Lett. **365**, 97–107 (2013)
30. T. Sakamaki et al., Earth Planet. Sci. Lett. **287**, 293–297 (2009)
31. https://earthref.org/GERMRD/datamodel/ (cit. on pp. 114, 115)
32. A. Donini, S. Palomares-Ruiz, J. Salvado, Nat. Phys. **15**, 37 (2019). [arXiv:1803.05901 [hep-ph]]
33. C. Rott, A. Taketa, D. Bose, Sci. Rep. **5**, 15225 (2015). [arXiv:1502.04930 [physics.geo-ph]]
34. S. Bourret, J. Coelho, E. Kaminski, V. Van Elewyck, PoS ICRC2019 (2020), 1024. https://doi.org/10.22323/1.358.1024
35. T.K. Gaisser, M. Honda, Ann. Rev. Nucl. Part. Sci. **52**, 153 (2002). [arXiv:hep-ph/0203272]
36. M. Honda, M. Sajjad Athar, T. Kajita, K. Kasahara, S. Midorikawa, Phys. Rev. D **92**, 023004 (2015). [arXiv:1502.03916]
37. R. Abbasi et al., [IceCube Collab.], Astropart. Phys. **35**, 615 (2012)
38. M.G. Aartsen et al., [IceCube Collab.], Phys. Rev. Lett. **120**, 071801 (2018)
39. P. Eller et al., [IceCube], PoS **ICRC2023**, 1036 (2023). arXiv:2307.15295
40. J.A. Sanchez [IceCube Collab], talk given at the International Conference on Neutrino Physics and Astrophysics, June 17–22, Milano, Italy (2024)
41. S. Adrian-Martinez, et al., [KM3Net], Letter of intent for KM3NeT 2.0. J. Phys. G **43**, 084001 (2016). arXiv:1601.07459
42. K. Abe et al., [Hyper-Kamiokande], “Hyper-Kamiokande Design Report.” arXiv:1805.04163
43. S. Muriyama [on behalf of the Hyper-Kamiokande Collab.], talk given at the XXX1 Int. Conference on Neutrino Physics and Astrophysics, June 16–22, Milano, Italy (2024)
44. B. Abi et al., [DUNE]. arXiv:1807.10334 [physics.ins-det]
45. S. Ahmed et al., [ICAL], Pramana **88**, 79 (2017). arXiv:1505.07380
46. M.G. Aartsen et al., [IceCube], Phys. Rev. Lett. **117**, 071801 (2016). arXiv:1605.01990
47. B. Luzum et al., Celest. Mech. Phys. **110**, 110 (2011)
48. H.USAO, USNO, UKHO, “The Astronomical Almanac”, http://asa.usno.navy.mil/
49. S.K. Agarwalla, T. Li, O. Mena, S. Palomares-Ruiz, arXiv:1212.2238
50. W. Winter, Nucl. Phys. B **908**, 250–267 (2016). https://doi.org/10.1016/j.nuclphysb.2016.03.033. [arXiv:1511.05154 [hep-ph]]
51. S. Bourret et al., [KM3NeT], J. Phys. Conf. Ser. **888**(1), 012114 (2017). https://doi.org/10.1088/1742-6596/888/1/012114. arXiv:1702.03723 [physics.ins-det]
52. A. Kumar, S. Kumar Agarwalla, arXiv:2104.11740
53. F. Capozzi, S.T. Petcov, Eur. Phys. J. C **82**, 461 (2022). [arXiv:2111.13048]
54. K.J. Kelly, P.A.N. Machado, I. Martinez-Soler, Y.F. Perez-Gonzalez, DUNE atmospheric neutrinos: Earth tomography. JHEP **05**, 187 (2022). [arXiv:2110.00003]
55. P.B. Denton, R. Pestes, Phys. Rev. D **104**, 113007 (2021). [arXiv:2110.01148]
56. L. Maderer, E. Kaminski, J.A.B. Coelho, S. Bourret, V. Van Elewyck, Front. Earth Sci. **11**, 1008396 (2023). arXiv:2208.00532
57. A.K. Upadhyay, A. Kumar, S.K. Agarwalla, A. Dighe, JHEP **04**, 068 (2023). arXiv:2211.08688
58. D. Raikwal, S. Choubey, Phys. Rev. D **109**, 073011 (2024). arXiv:2309.12573
59. A.K. Upadhyay, A. Kumar, S.K. Agarwalla, A. Dighe, arXiv:2405.04986
60. S. Choubey, P. Ghoshal, S.T. Petcov, studies performed in the period 2008–2011 for the 100 kt liquid Argon and 1 Mt water Cerenkov (Hyper-Kamiokande) detectors, unpublished
61. S. Choubey, S.T. Petcov, studies performed in 2014 for the PINGU detector, unpublished
62. T. Ohlsson, W. Winter, Phys. Lett. B **512**, 357 (2001). arXiv:hep-ph/0105293
63. S.T. Petcov, Eur. Phys. J. C **84**, 991 (2024). arXiv:2406.13727 [hep-ph]
64. S.T. Petcov, Phys. Lett. B **434**, 321 (1998). https://doi.org/10.1016/S0370-2693(98)00742-4. arXiv:hep-ph/9805262
65. M.V. Chizhov, S.T. Petcov, Phys. Rev. Lett. **83**, 1096 (1999). arXiv:hep-ph/9903399
66. M.V. Chizhov, S.T. Petcov, Phys. Rev. D **63**, 073003 (2001). arXiv:hep-ph/9903424
67. M. Chizhov, M. Maris, S.T. Petcov, arXiv:hep-ph/9810501
68. E.K. Akhmedov, M. Maltoni, A.Y. Smirnov, JHEP **05**, 077 (2007). arXiv:hep-ph/0612285
69. E.K. Akhmedov, M. Maltoni, A.Y. Smirnov, Phys. Rev. Lett. **95**, 211801 (2005). arXiv:hep-ph/0506064
70. L. Wolfenstein, Phys. Rev. D **17**, 2369 (1978)
71. V. Barger et al., Phys. Rev. D **22**, 2718 (1980)
72. P. Langacker, J.P. Leveille, J. Sheiman, Phys. Rev. D **27**, 1228 (1983)
73. S.P. Mikheev, A.Y. Smirnov, Sov. J. Nucl. Phys. **42**, 913 (1985)
74. T. Wester et al. [Super-Kamiokande Collaboration], Atmospheric neutrino oscillation analysis with neutron tagging and an expanded fiducial volume in Super-Kamiokande I-V. Phys. Rev. D **109**(7), 072014 (2024). https://doi.org/10.1103/PhysRevD.109.072014. arXiv:2311.05105 [hep-ex]
75. W. Chen, J. Ray, W.B. Shen, C.L. Huang, J. Geod. **89**, 179 (2015)
76. Super-Kamiokande Collaboration, “Data release: Atmospheric neutrino oscillation analysis with neutron tagging and an expanded fiducial volume in Super-Kamiokande I-V,” Zenodo, (2023). https://doi.org/10.5281/zenodo.8401262
77. M. Honda, T. Kajita, K. Kasahara, S. Midorikawa, Improvement of low energy atmospheric neutrino flux calculation using the JAM nuclear interaction model. Phys. Rev. D **83**, 123001 (2011). https://doi.org/10.1103/PhysRevD.83.123001. arXiv:1102.2688 [astro-ph.HE]
78. Y. Hayato, A neutrino interaction simulation program library NEUT. Acta Phys. Pol. B **40**, 2477–2489 (2009)
79. Y. Hayato, L. Pickering, The NEUT neutrino interaction simulation program library. Eur. Phys. J. ST **230**(24), 4469–4481 (2021). https://doi.org/10.1140/epjs/s11734-021-00287-7. arXiv:2106.15809 [hep-ph]
80. F.N. Fritsch, J. Butland, A method for constructing local monotone piecewise cubic interpolants. SIAM J. Sci. Stat. Comput. **5**(2), 300–304 (1984)
81. I. Esteban, M.C. Gonzalez-Garcia, M. Maltoni, I. Martinez-Soler, J.P. Pinheiro, T. Schwetz, arXiv:2410.05380 [hep-ph]
82. Proc. of the 8th International Conference on Neutrino Physics and Astrophysics - “Neutrino’78” ed. by E.C. Fowler (Purdue University Press, West Lafayette, 1978), p. C3